1   **The unique features in the four-day widespread extreme rainfall event over North**

2   **China in July 2023**

4   Jinfang Yin[1,2,3], Feng Li[1], Mingxin Li[1], Rudi Xia[1], Xinghua Bao[1],

5   Jisong Sun[1], and Xudong Liang[1]

7   [1] State Key Laboratory of Severe Weather, Chinese Academy of Meteorological

8   Sciences, Beijing 100081, China

9   [2] Research Center for Disastrous Weather over Hengduan Mountains & Low-Latitude

10   Plateau, China Meteorological Administration (CMA), Kunming 650034, China

11   [3] Shigatse National Climatological Observatory, CMA, Shigatse 857000, China

13   Submitted to *Natural Hazards and Earth System Sciences* (*NHESS*)

14   August 2024

15   Second round November 2024

17   Corresponding author: Jinfang YIN

18   E-mail: yinjf@cma.gov.cn

ABSTRACT

20   Synoptic forcings have traditionally played a pivotal role in extreme rainfall over North

21   China. However, there are still large unexplained gaps in understanding the formation of

22   extreme rainfalls over this region. The heavy rainfall event, lasting from 29 July to 2 August

23   2023 (referred to as "23·7" event), is characterized by long duration, widespread coverage,

24   and high accumulated rainfall over North China. Overall, the persistent extreme rainfall is

25   closely associated with the remnant vortex originating from typhoon Doksuri (2305), tropical

26   storm Khanun (2306), and the unusual westward extended Western North Pacific Subtropical

27   High (WNPSH), as well as quasi-stationary cold dry air masses surrounding North China on

28   the west and north sides. Based on wind profiles and rainfall characteristics, the life history of

29   the "23·7" event is divided into two stages. In the first stage, the western boundary of the

30   WNPSH was destroyed by the tropical storm Doksuri, appearing that the WNPSH retreated

31   eastward with decreasing height. As a result, an inclined vertical distribution on the western

32   boundary was established below 500 hPa. Therefore, convections were limited by the tilted

33   WNPSH with warm-dry cover embedded in the low-to-middle troposphere. Meanwhile, the

34   orography in the west of North China was controlled by cold air masses above nearly 3.0 km.

35   Combining the orographic and cold air blockings, only a shallow southeasterly layer

36   (between 1.3 and 3.0 km) can overpass mountains. Although the warm and moist

37   southeasterly flows were lifted by orography, no convections were triggered because of the

38   local capped cold and dry air masses overhead. Under this framework, equivalent potential

39   temperature (θ_e) gradients were established between warm humid and dry cold air masses,

40   similar to a warm front, causing warm air to lift and generate widespread rainfall but low

41   intensity. However, the lifting was too weak to allow convection to be highly organized. In the

42   second stage, the WNPSH was further destroyed by enhanced Khanun, and thus the

43   embedded warm-dry cover associated with the tilted WNPSH was significantly thinned.

44   Consequently, convections triggered by orographic blocking can move upward and

45   consequently further develop, forming deep convections. Comparatively speaking, the

46   convections in the second stage are much deeper than those in the first stage. The results

47   gained herein may shed new light on better understanding and forecasting of long-lasting

48   extreme rainfall.

1. Introduction

A persistent severe rainfall event occurred over central and North China during the period from 29 July to 2 August 2023 (referred to as "23·7" event), which was regarded as one of the precipitation extremes of 2023 globally (Fowler et al., 2024). Despite the rainfall in low intensity, it was long-lasting and widespread, resulting in large accumulated rainfall. Overall, the average accumulated rainfall over North China (including Beijing, Tianjin, and Hebei Province) was 175 mm, which was approximately 1/3 of the average annual precipitation in this region. Flooding from this event affected 1.3 million people, bringing severe human casualties and economic losses. The sustained severe rainfall over Beijing left 33 people dead and 18 missing persons. One of the distinct features of this rainfall event was closely associated with the remnant vortex originating from typhoon Doksuri (2305), tropical storm Khanun (2306), unusual westward extended Western North Pacific Subtropical High (WNPSH), and quasi-stationary cold dry air masses surrounding North China on their west and north sides.

It is common for rainfall occurrence over North China due to strong water vapor supply by tropical cyclones over the East China Sea and/or Southern China Sea (e.g., Ding,1978; Feng and Cheng,2002; Yin et al.,2022c). Like the "96·8" severe rainfall event (Sun et al.,2006; Bao et al., 2024), the present persistent rainfall event was closely linked to two tropical storms of Doksuri (2305) and Khanun (2306). Note that the Doksuri weakened to a typhoon remnant vortex (typhoon-low pressure) at this moment as it moved inland after landfalling, while the tropical storm Khanun was in a fast-developing stage. The tropical storm Khanun and the typhoon remnant vortex built jointly a water vapor bridge, transporting a large amount of water vapor to North China from the East China Sea. Previous studies (e.g., Hirata and Kawamura, 2014; Gao et al.,2022; Yang et al.,2017) pointed out that large amounts of water vapor brought by a typhoon over the North Pacific were favorable for severe rainfall generation in eastern China.

In the last several decades, considerable attention was paid to the remote rainfall events associated with tropical cyclones, with substantial progress made (e.g., Wang et al.,2009; Xu et al.,2023a; Xu et al.,2023b; Lin and Wu,2021). Commonly, sufficient water vapor provided by a tropical cyclone plays an important role in extreme rainfall over North China (e.g., Rao et al.,

2023; Xu et al.,2023b). Besides, many studies confirmed that the WNPSH is closely related to water vapor transportation and the spatial distribution of rainfall (e.g., Hu et al.,2019; Gao et al., 2022). Additionally, orographic forcing of the approaching warm and moist unstable airflow plays a critical role in determining the location of convection initialization, although sometimes orographic forcing played a small role compared to Typhoon's circulation (Wang et al.,2009). Moreover, severe rainfall can be generated by the complicated cloud microphysical processes due to the interactions between tropical oceanic warm-moist and mid-latitude cold-dry air masses (Wang et al.,2009; Xu and Li,2017; Xu et al.,2021). Despite some experiences gained, there are still large unexplained gaps in understanding the formation of extreme rainfall (Meng et al.,2019).

Due to the tremendous impacts of the "23·7" event, many scholars have carried out studies of the event from various aspects. Li et al (2024) provided a detailed analysis of fine characteristics of the precipitation using radar and dense rain gauge observations. Xia et al. (2025) investigated extreme hourly rainfalls at different episodes. Fu et al. (2023) paid attention to the effects of dynamic and thermodynamic conditions on precipitation, while Gao et al. (2024) focused on the impact of mountain-plain thermal contrast on precipitation distribution. Although operational forecasts gave a reasonable spatial distribution of precipitation at that time, the precipitation intensity was underestimated significantly. Indeed, it is found that, in this event, the unusual westward-extended WNPSH played an important role in modulating convection initialization and development with several unusual features revealed. However, given the unusual westward-extended WNPSH, some unexplainable questions have been raised, while little attention has been paid to date. Firstly, what mechanism(s) could account for the persistent severe rainfall? Besides, what is the role of the unusual westward-extended WNPSH in governing the rainfall over North China? Therefore, we are motivated to conduct the present modeling study to answer those questions.

The rest of the paper is organized as follows. A detailed description of the main features of extreme rainfall and synoptic-scale weather conditions is documented. Section 3 provides detailed model configuration and verification against observations. We present a detailed analysis of the extreme rainfall production in Section 4. The paper finishes with conclusions

107 and outlooks.

2. Properties of rainfall and wind profiles

2.1 Characteristics of rainfall

Figure 1 shows the spatial distribution of 96-h accumulated rainfall from observations during the period from 0000 UTC 29 July to 0000 UTC 2 August 2023, with the peak amount of 1004 mm at Liangjiazhuang station near Xingtai, Hebei Province of North China. Exceptionally long duration of rainfall is a notable feature of the event, with the longest duration being 80 hours within the four days at some stations. The spatial distribution of the rain belt with three severe rainfall cores is consistent with the orography direction of the Yanshan Mountains on the north as well as of the Taihang Mountains on the south, suggesting that orography plays an important role in the precipitation. It should be emphasized that three rainfall cores, marked by Mentougou (MTG, 741 mm) in Beijing, and Yixian (YX, 753 mm) and Xingtai (XT, 1004 mm) in Hebei Province, correspond respectively to the regions with large topographic gradients (Fig. 1). Please refer to Li et al. (2024) for a detailed analysis of fine features of this rainfall event.
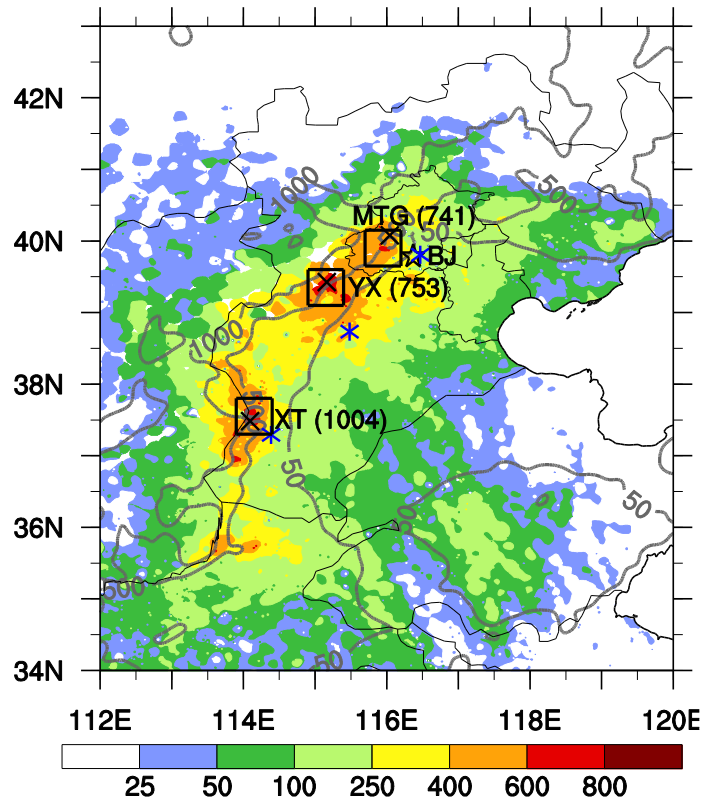
Fig. 1 Spatial distribution of 96-h accumulated rainfall (mm, shadings) from the intensive surface rain gauge observations during the period from 0000 UTC 29 July to 0000 UTC 2

August 2023; Gray contours denote orography from 50 m to 1000 m as marked. Three rainfall cores in Mentougou (MTG) in Beijing, and Yixian (YX) and Xingtai (XT) in Hebei Province are denoted by squares, with the values in parentheses indicating the maximum accumulated rainfall (marked by crisscross sign ×) for the regions, respectively. The blue asterisks (∗) represent the locations of wind profiler observational stations near the three rainfall cores. The start (☆) sign indicates the location of Beijing (BJ) City. (Similarly for the rest of figures).

2.2 Wind profiles

The observed wind profiles near MTG, YX, and XT are shown in Fig. 2. It is found that temporal variations in horizontal wind fields are distinct during the rainfall event. Taking the wind profiles near MTG as an example (Fig. 2a), the easterly or southeasterly wind at the levels below 4 km was increased gradually from 2 m s^{-1} at 1200 UTC 28 to 24 m s^{-1} at 1200 UTC 30 July 2023. The easterly or southeasterly wind lasted to 0400 UTC 31 July 2023, turned southerly except for near the ground, and then turned southwesterly near 0400 UTC 1 August 2023. After 0400 UTC 31 July, wind speed decreased significantly and then increased drastically. More specifically, the wind speed was decreased from 8 m s^{-1} to 2 m s^{-1}, and then increased to 14 m s^{-1} near 1 km above the ground. However, opposite variations were observed above 4 km. One can see that the horizontal wind shifted from southwesterly to southerly, then back to southwesterly. Overall, the shift in wind direction and speed altered the vertical wind shear, which directly affected the development and organization of subsequent convection (Pucik et al., 2021). Similar variations can also be found at YX and XT stations, although the timing of changes is not synchronized with each other (Fig. 2c, d). The variations proceeded from south to north, starting first at XT and finally at MTG, in pace with the typhoon moving from south to north.

148
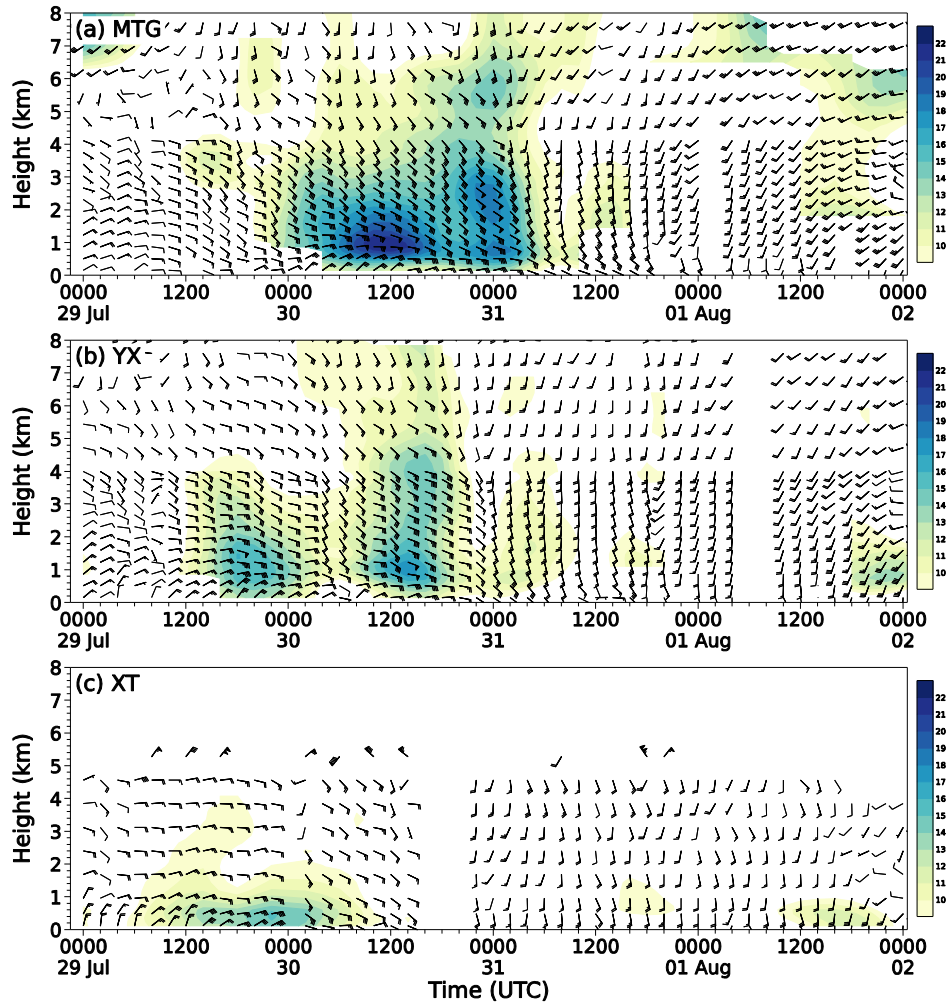
Fig. 2 Temporal evolution of the wind profile (a full barb is 4 m s^{-1}, and shadings denote wind speed over 10 m s^{-1}) from observations near (a) MTG, (b) YX, and (c) XT during the period of 0000 UTC 29 July to 0000 UTC 2 August 2023. Note that only the wind profile below 5 km above the ground is able to be observed due to the limitation of the instrumentation near Xingtai (XT). (see Fig. 1 their locations).

2.3 Synoptic conditions on 28 July 2023

Figure 3 displays a weather chart on 500 hPa at 1200 UTC 28 July 2023. One can see that the large-scale flow patterns exhibited a coexistence of the tropical storm Khanun (2306) with a remnant vortex originating from typhoon Doksuri (2305)[*]. Note that the Khanun was in the rapid development stage then, while the vortex weakened significantly at that time. Another important weather system was the WNPSH (denoted by the 588 isoline) with a square-head

---

[*]The typhoon Doksur i(2305) weakened to a typhoon remnant vortex as it was passing through East China's Anhui Province. The China Meteorological Administration (CMA) stopped issuing updates on the Doksuri at 0300 UTC 29 July 2023. The remnant of Doksuri remained in a vortex in the lower troposphere, although its wind force diminished as it moved northward.

160 shape on its western border. Clearly, a water vapor transportation passage was built due to the

161 cyclonic circulation of the tropical storm in combination with the anticyclonic circulation on

162 the southwestern part of the WNPSH. As a result, central and North China was covered by high

163 precipitable water (PW) of over 68 mm. Similar patterns can be viewed at the level of 850 hPa

164 (not shown).
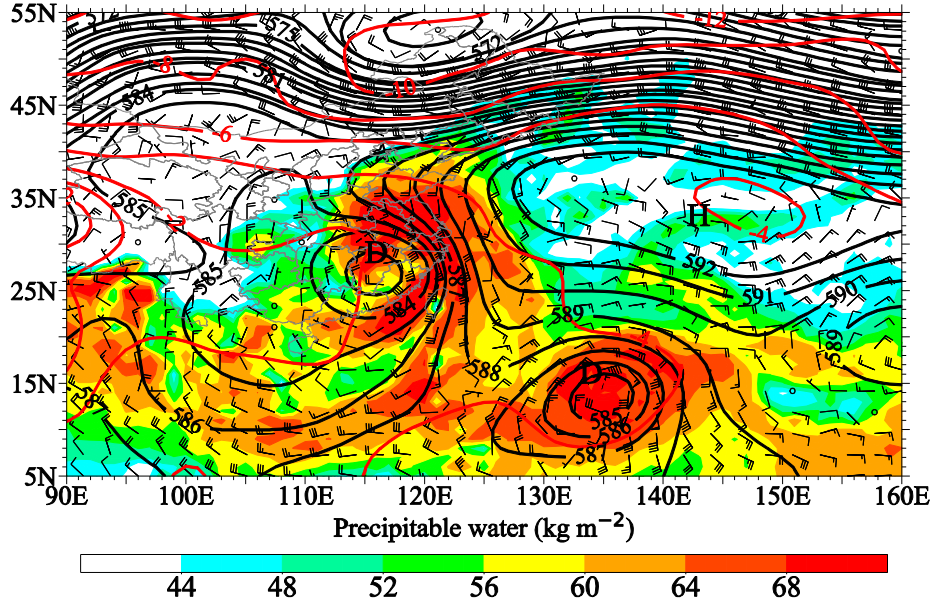
165
166 **Fig. 3** Weather chart on 500 hPa at 1200 UTC 28 July 2023: Geopotential height

167 (black-contoured at 15 gpm intervals), temperature (red-contoured at 2°C intervals), wind barbs

168 (a full barb is 4 m s^{-1}), and precipitable water (kg m^{-2}, shadings).

169 **3. Model configuration and verification**

170 *3.1 Model description*

171   In this study, the persistent severe rainfall event is reproduced with the WRF model

172 version 4.1.3. The WRF model is configured in two-way nested grids of horizontal grid sizes of

173 9 km, 3 km, and 1 km. Figure 4 displays the geographical coverage of the WRF model domains,

174 with the grid points of 901(nx)×601(ny), 973×1231, and 1231×1591 for the outer, intermediate,

175 and inner domains, respectively. The outermost domain (i.e., D01) is centered at 115°E, 35°N,

176 and a total sum of 58 sigma levels is assigned in the vertical with the model top fixed at 20 hPa.

177 Since the rainfall is closely associated with the spatial distribution of orography over North

178 China (Fig. 1), the Shuttle Radar Topography Mission (SRTM) high-resolution (90 m)

179 topographic data is employed in the present simulation. It should be noticed that the model

180 vertical level distribution was carefully tested and has achieved good performance (Yin et al.,

181 2020; Yin et al.,2022a; Yin et al.,2018; Yin et al.,2022b). The WRF model physics schemes are

182 configured with the YSU scheme for the planetary boundary layer (Hong et al., 2006), and the

183 revised MM5 Monin-Obukhov (Jimenez) scheme for the surface layer (Jiménez et al., 2012),
184 as well as the Unified Noah Land Surface Model (Tewari et al.,2004). The rapid radiative
185 transfer model (RRTM) (Mlawer et al.,1997) and the Dudhia scheme (Dudhia,1989) are used
186 for longwave and shortwave radiative flux calculations, respectively. The Kain-Fritsch cumulus
187 parameterization scheme (Kain,2004) is utilized for the outer two coarse-resolution domains
188 but is bypassed in the finest domain (i.e., D03). The Thompson-ensemble cloud microphysics
189 scheme is applied to the explicit cloud processes (Thompson et al.,2008; Yin et al.,2022a).
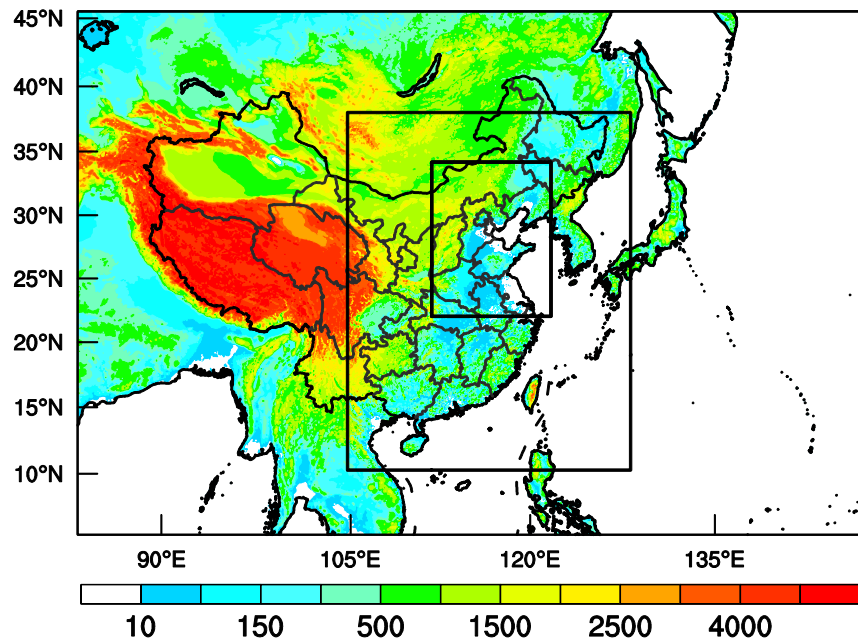
190
191 **Fig. 4** The WRF model orography (m, shadings) and the nested model domains used for
192 simulations with the grid sizes of 9 km (D01), 3 km (D02), and 1 km (D03).

193   The WRF model is integrated for 108 hours, starting from 1200 UTC 28 July 2023, with
194 outputs at 6-min intervals. The model outputs in the first 12 h are considered as the spin-up
195 process and thus are not used for the present work. The initial and outermost boundary
196 conditions are interpolated from the final operational global analysis of 1-degree by 1-degree
197 data at 6-h intervals from the Global Forecasting System of the National Centers for
198 Environment Prediction (NCEP). In order to force large-scale fields consistent with the driving
199 fields, grid analysis nudging is activated by performing the Four-Dimension Data Assimilation
200 (FDDA) throughout the model integration (Bowden et al.,2012; Stauffer et al.,1991). The
201 innermost domain (i.e., D03) outputs are validated and used for further analysis, and the
202 outermost domain (i.e., D01) outputs are used to demonstrate weather-scale dynamical and
203 thermal features. The wind profiler and surface hourly observations are provided by the
204 National Meteorological Information Center (NMIC) of the China Meteorological

205 Administration (CMA) after strict quality control.

3.2 Model verification

207 Figure 5 shows the spatial distribution of 96-h accumulated rainfall from the simulation
208 during the period from 0000 UTC 29 July to 0000 UTC 02 August 2023. Generally speaking,
209 the WRF model replicates well the spatial distribution of severe rainfall. The rainfall belt with
210 three rainfall cores coinciding with the orography is reproduced well, and the simulated
211 extreme rainfall amount matches well with the observed. Note that the model produces a peak
212 96-h accumulated rainfall of 778 mm over the XT region, while the maximum rainfall of 1004
213 mm was observed over the XT region. Despite the simulation underestimates rainfall over this
214 region, it captures the main features of rainfall over central and North China.
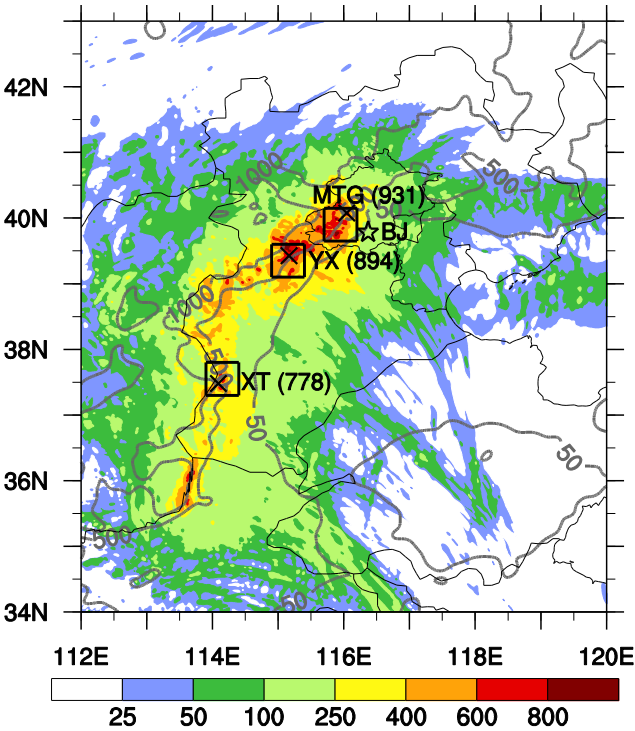
Fig. 5 Same as in Fig. 1 but for the simulated rainfall (mm, shadings).

217 Figure 6 compares the spatial distribution of daily rainfalls between observations and
218 simulations during the period from 0000 UTC 30 July to 0000 UTC 2 August 2023. From
219 observations, one can see that the daily rainfalls show obvious variations. On the first day (Fig.
220 6a), the rainfall occurred mainly in northern Henan Province and southern Hebei Province, on
221 the east side of the Taihang Mountains with the rainfall cores over 250 mm. On the next day
222 (Fig. 6b), the rainfall extended significantly northeastward, and a new strong rainfall core
223 occurred, covering central Hebei Province and southwest Beijing. On the third day (Fig. 6c),

224 rainfall was significantly reduced in both coverage and intensity, mainly occurring in Beijing

225 and the surrounding areas. On the fourth day (Fig. 6d), rainfall moved eastward and weakened

226 rapidly. It is apparent that the model reproduces well the evolutions of the rainfall (Fig. 6e-h),

227 with general characteristics similar to the observed (Fig. 6a-d).

228

229
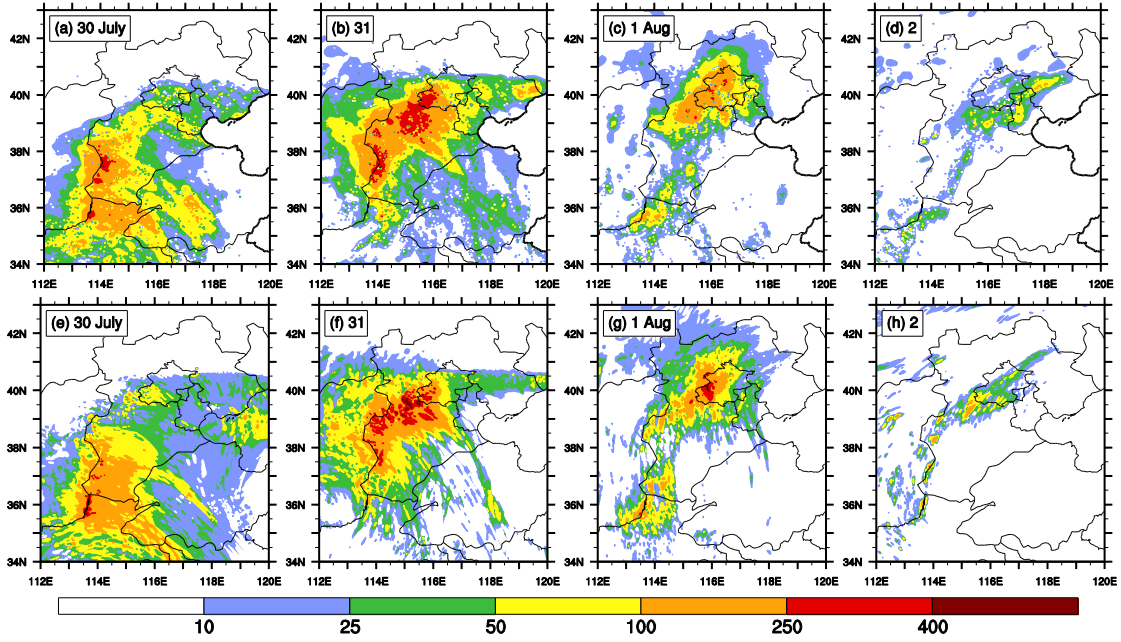
230 **Fig. 6** Spatial distribution of (a-d) observed and (e-h) simulated daily rainfall (mm) during the

231 period from 0000 UTC 30 July to 0000 UTC 2 August 2023.

232   Figure 7 compares the time series of hourly rainfall rates between the observed and the

233 simulated over the MTG, YX, and XT regions. The rainfall event is characterized by long

234 duration, widespread coverage, and high intensity. As has been mentioned above, the rainfall

235 extended from the south to the north, covering Henan Province, Hebei Province, and Beijing.

236 The rainfall first occurred in the XT region and ended near 0000 UTC 31 July 2023. In the wake

237 of that the rainfall belt moved northeastward, over both the MTG and YX regions rainfall

238 occurred, and it ended nearly at 0000 UTC 2 August. The observed timings of initiating and

239 ending of the rainfall event are well replicated by the WRF model, with the observed peaks

240 reproduced as well, although there are some timing biases. For example, the strongest rainfall

241 occurred over the MTG region during the period from 0000 UTC to 0600 UTC 31 July.

242 However, the simulated strongest rainfall has a 6-h lag, occurring from nearly 0600 UTC to

243 1200 UTC 31 July depending on the region. Overall, good agreements between the simulation

244 and observations are obtained in terms of the timing and location in the spatial distribution of

245 rainfall.

246
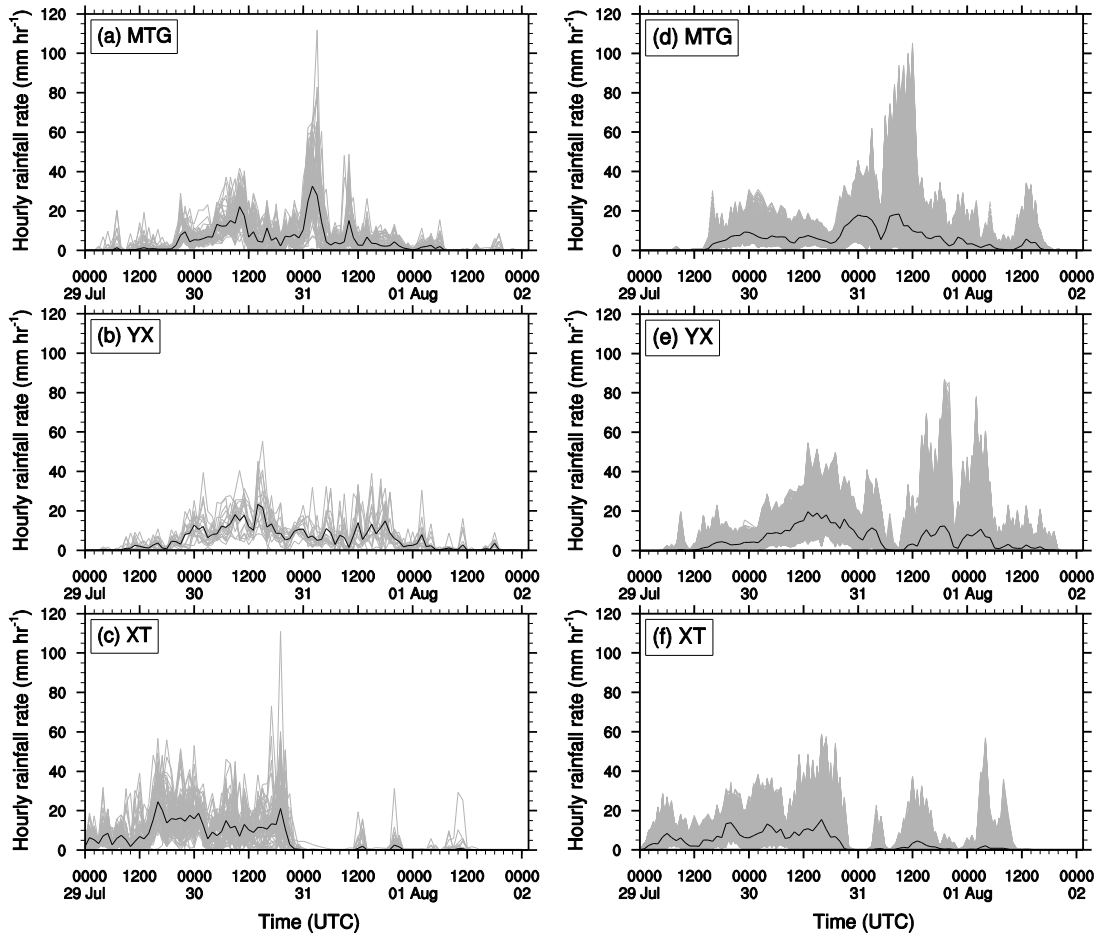
Fig. 7 Time series of (a-c) the rain gauge observations and (d-f) the simulated hourly rainfall rates (gray lines, mm hr^{-1}) for all the stations/grid points over the (a, d) MTG, (b,e) YX, and (c,f) XT regions during the period of 0000 UTC 29 July to 0000 UTC 02 August 2023. The black line denotes the domain-averaged hourly rainfall rates over all the stations (grid points) from observations (simulations). (see Fig. 1 for their locations). In total, 74, 19, and 67 observations are used for (a) MTG, (b) YX, and (c) XT, respectively. For the simulation, there are (d) 2296, (e) 2365, and (f) 2420 grid points, respectively.

The evolution of the simulated wind profile is presented in Fig. 8. Similar to the observed (Fig. 2), the simulated easterly wind increased gradually from nearly 1200 UTC 29 July, corresponding to the start of the precipitation (Fig. 6e-h). The horizontal wind shifted from easterly to southerly except for near the ground and then turned to southwesterly with wind speed decreasing significantly. Overall, the variations of the simulated wind profile were consistent with those observed, indicating that the WRF model was able to well capture the main features of the wind profile. Based on the wind profile and rainfall features, the simulated

261   rainfall process is roughly divided into two stages. The shift moments (roughly marked by thick

262   black lines) are near at 0800 UTC 31, 2000 UTC 30, and 1600 UTC 30 July for the MTG, YX,

263   and XT regions, respectively. It should be noted that the wind field was significantly

264   influenced by Typhoon Khanun (2306) and the remnant vortex originating from Typhoon

265   Doksuri (2305) in the present event. As the typhoon gradually moved northwestward and the

266   vortex weakened, the first region to be affected was Xingtai (XT) in the south, then Yixian

267   (YX) in the center, and finally Mentougou (MTG) in the north, suggesting that the wind shift

268   occurred at a different moment.
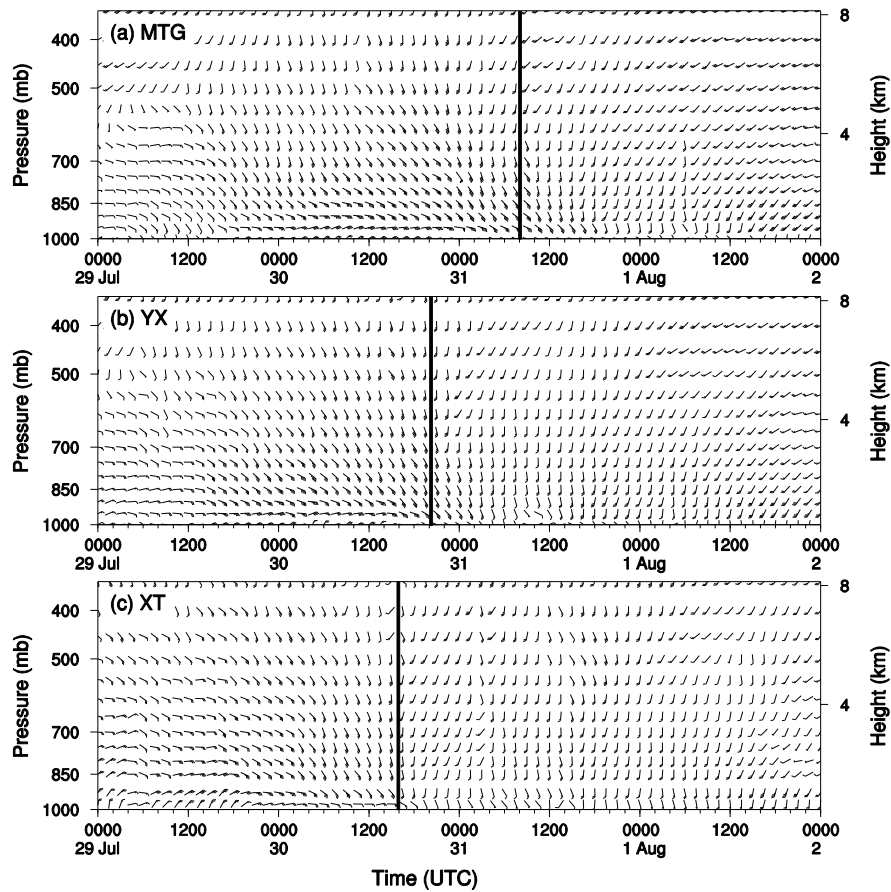
269
270 **Fig. 8** Same as Fig. 2 but for the simulated. The black lines denote wind shift from

271 southeasterly to southerly/southwesterly over the levels in the low to middle troposphere,

272 which roughly divided the rainfall event into two stages.

273 **4. Unique features for the extreme rainfall**

274 *4.1 Dominant dynamic processes for convection initialization*

275   The evolution of dynamical and thermal systems of the rainfall event in the first stage is

276 shown in Fig. 9. Although only a remnant vortex remained over central China at this time,

277 typhoon Doksuri had an important influence on the WNPSH when it was strong as a super

278   typhoon. Several days before the rainfall event, the super typhoon Doksuri was close to the

279   WNPSH, and the southwest WNPSH edge was within the typhoon's outer region. Owing to the

280   inflow mass flux entering the typhoon region, the southwest part of WNPSH was severely

281   weakened by typhoon Doksuri (Sun et al.,2015). As a result, the west boundary of the WNPSH

282   appeared to an eastward retreat from 500 hPa to 850 hPa, showing an inclined vertical

283   distribution on its western boundary, especially from 700 hPa to 850 hPa. Capped by the

284   inclined WNPSH, water vapor was mainly transported to North China through a passage nearly

285   under 850 hPa that is built by the typhoon remnant vortex combined with the tropical storm

286   Khanun. At 500 hPa (Fig. 9a), the WNPSH (represented by the 588 isoline) covered a large part

287   of eastern China, with an unusual westward extension of the northwest corner to northwestern

288   China. At that time, the northwest corner extended much further westward, compared to that

289   before 12-h (Fig. 3). Similar patterns can be seen at 700 hPa (Fig. 9b), but the west boundary of

290   WNPSH (represented by the 316 isoline) retreated to the East China Sea except for the

291   northwest corner. At 850 hPa (Fig. 9c), the WNPSH (represented by the 156 isoline) completely

292   retreated to the Western North Pacific, far away from China.

293   The spatial distribution of the high PW was consistent with that of a large equivalent

294   potential temperature (θ_e) of 344K at 500 hPa, indicating that the 334K contour covered a

295   relatively warm and/or wet region (Fig. 9a). Most importantly, the boundary of the high PW

296   corresponded to the large value of the potential temperature gradient over 8K on the east side

297   and 12K on both north and west sides. Previous studies (e.g., Rao et al.,2023) proposed that the

298   heavy rainfall region was closely attributed to the distributions of θ_e. Although the warm and

299   moist conditions were favorable for precipitation, the unfavorable large-scale forcings explain

300   well why no deep convection was formed over this region (marked with a dashed-line box in

301   Fig. 9c, d). The convergence, resulting from changes in wind direction and wind speed, was

302   conducive to triggering convection. Consequently, the weak convergence led to weak lifting

303   and consequent precipitation. Since the convergence occurred at the junction of cold and warm

304   air masses, like a warm front rainfall, rainfalls were formed in low intensity but long duration

305   and widespread coverage. It is important to note that the spatial distribution of rainfall is usually

306   considered to be consistent with the western boundary of WNPSH (i.e., the 588 isoline) at 500

307   hPa. However, the spatial distribution of rainfall in the present event is consistent with the dense

308   zone of θ_e, instead of the western boundary of WNPSH. Therefore, in addition to the isoline 588

309   at 500 hPa, the spatial distribution of θ_e needs to be given more attention in future operational

310   forecasts.
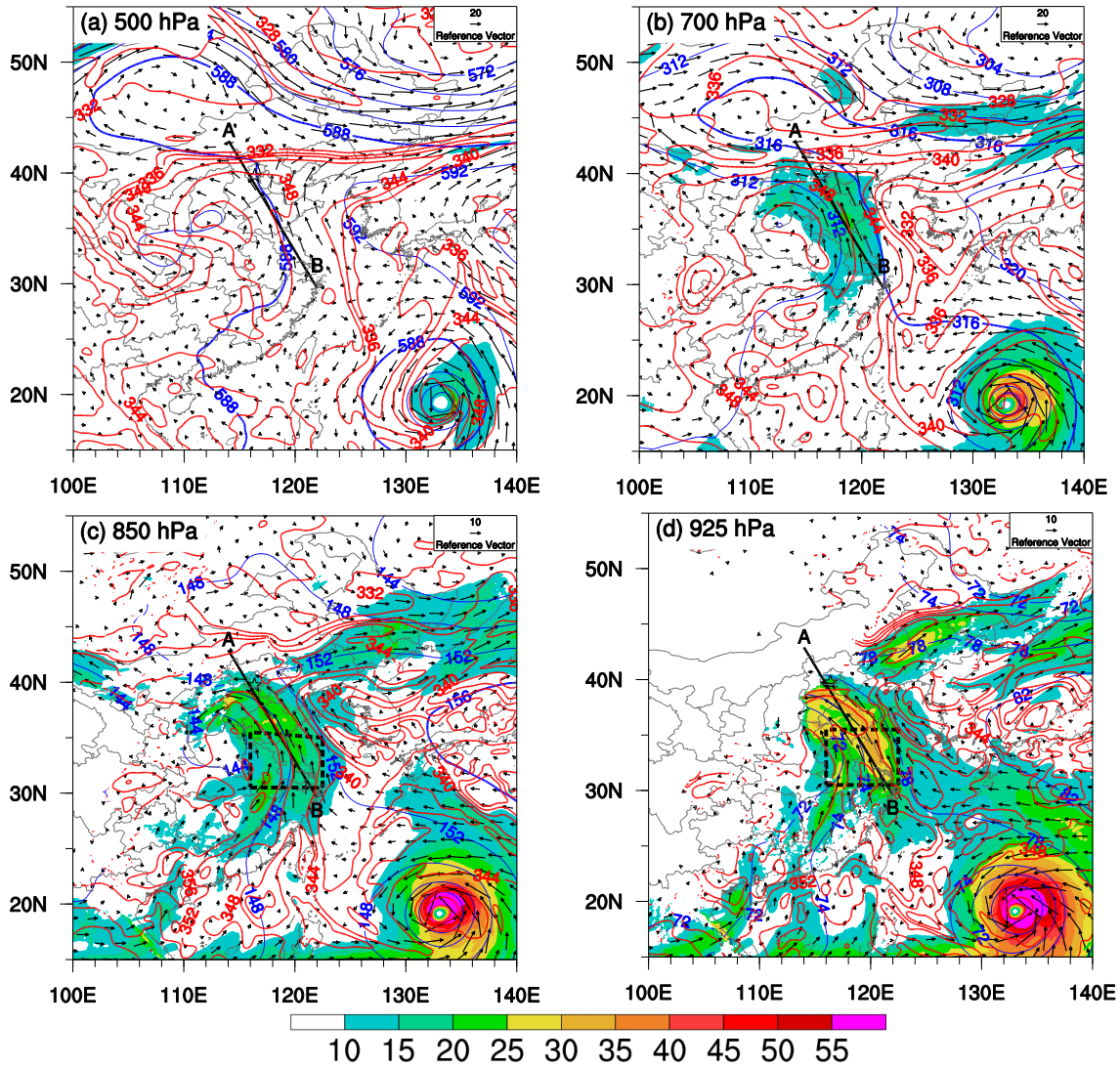
311   **Fig. 9** Spatial distribution of geopotential height (blue contoured at 40 gpm), equivalent

312   potential temperature (red contoured at 2K intervals, θ_e), wind bars (a full barb is 4 m s^{-1}), and

313   water vapor flux (g s^{-1} cm^{-1} hPa^{-1}, shadings) from the model D01 at 0000 UCT 30 July 2023: (a)

314   500 hPa, (b) 700 hPa, (c) 850 hPa, and (d) 925 hPa. The isolines of 588, 316, and 156 are

315   bolded to represent the WNPSH at 500 hPa, 700 hPa, and 850 hPa, respectively. The

316   convergence zone of southeast and southwest flows is marked by a dashed line box in panels (c)

317   and (d). The thick black line A–B denotes the locations for cross-section along the water vapor

318   transport pathway used in Fig. 10.

319   The warm and moist features over North China can also be seen from the cross-section

320   along the line A–B as shown in Fig. 10. The western orography region was occupied by cold air

321   mass over the levels above 3.0 km. Under the conditions, significant equivalent potential

322   temperature gradients were established between the warm and cold air masses, similar to a

323   warm front. Meanwhile, owing to the blocking of orography below 1.3 km and the strong cold

324   air mass above 3.0 km, only the southeasterly flows between 1.3 and 3.0 km above the sea level

325   can overpass the mountains. It should be noted that although the warm and moist southeasterly

326   flows were lifted by the orography, they could not move further upward to trigger convection

327   because of the local capped cold and dry air masses overhead. Consequently, convergence

328   mainly resulted from the changes in wind direction and wind speed caused upward motion. As

329   the warm and moist air was lifted, condensation occurred and even generated precipitation. It

330   should be emphasized that the lifting was too weak to allow convection to be highly organized

331   (Fig. 10). For example, the updrafts in strong deep convective systems (e.g., Yin et al.,2020;

332   Yin et al.,2022c) are 5-10 times as large as the updrafts in the present event. Therefore, the weak

333   lifting was responsible for the rainfall in large coverage but low intensity. Besides, the

334   continuous and stable water vapor supply was another favorable factor for the precipitation.

335   Also from Fig. 10, one can see that North China was surrounded by warm dry air masses

336   on the east side and cold dry air masses on both north and west sides. More specifically, the air

337   mass at the levels above 1 km on the east side was over 3°C warmer than surrounding regions,

338   but the water vapor mixing ratio (q_v) was less than 14 g kg^{-1} (humidity was less than 70%)

339   because this region was controlled by the WNPSH. The warm-dry cap overhead explains well

340   the absence of convection and rainfall over this region (cf. Figs. 5 and 6). On the north and west

341   sides, the air masses were dry with q_v less than 2 g kg^{-1}. The air was over 3°C colder than the

342   surrounding region except for the air near the ground. In view that warm air near the ground

343   might be associated with radiative heating from the ground, owing to being capped by the cold

344   and dry air overhead, it would be understandable why convection could not be enhanced over

345   the mountains.
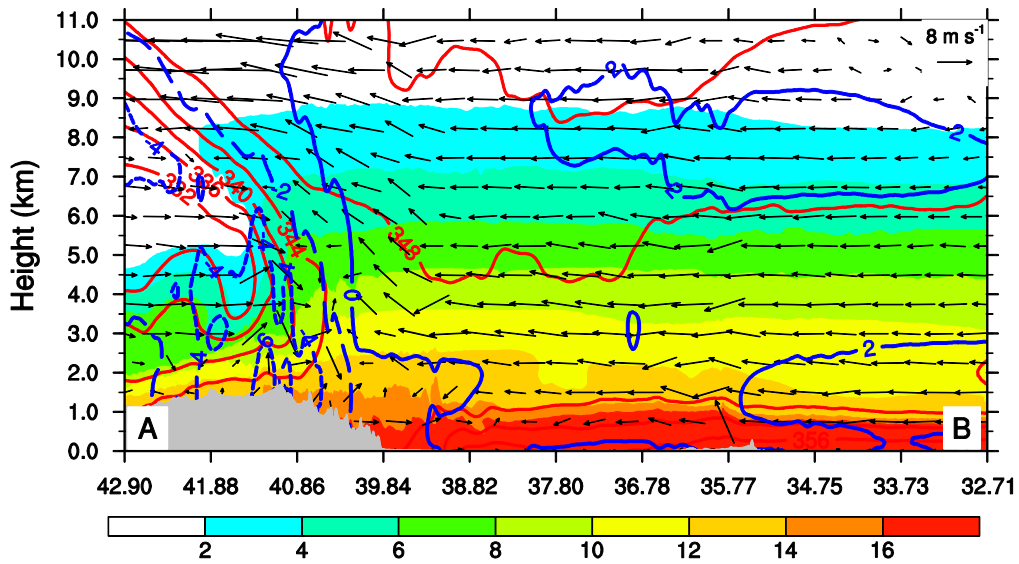
Fig. 10 Vertical cross-section along line A–B given in Fig. 9 of temperature deviations (blue-contoured at 2°C intervals) from their level-averaged values in the cross-section, equivalent potential temperature (red-contoured at 4K intervals), water vapor mixing ratio (q_v, g kg^{-1}, shadings), and in-plane flow vectors (vertical motion amplified by a factor of 20) at 0000 UCT 30 July 2023, respectively. Gray shadings denote terrain.

In the second stage (Fig. 11), obvious differences in dynamical and thermal processes can be seen, compared to those in the first stage (cf. Fig. 9). At 500 hPa (Fig. 11a), the WNPSH further expanded westward with its western border reaching western China. It should be emphasized that the southwestern part of WNPSH was severely damaged by the rapid intensification of Khanun into a super typhoon. Meanwhile, as the trough deepened over northeastern China, cold air from the north poured southward. Consequently, a north-south orientated θ_e dense zone was established over eastern China. Similar patterns in θ_e and horizontal wind field can be seen at 700 hPa (Fig. 11b). However, the WNPSH (represented by the 316 isoline) was further disrupted as the Khanun continued to intensify, appearing that the WNPSH retreated to the East China Sea except for the northwest corner. The north-south orientated θ_e dense zone greatly prevented water vapor from transporting to North China above 850 hPa, and thus water vapor was mainly transported to North China by a shallow southeasterly flow near the ground (Fig. 11c, d). Consequently, the water vapor flux was significantly reduced (Fig. 12a). Besides, North China was dominated by southerly flows over levels above 500 hPa, and thus mid-tropospheric wind shear was significantly enhanced.
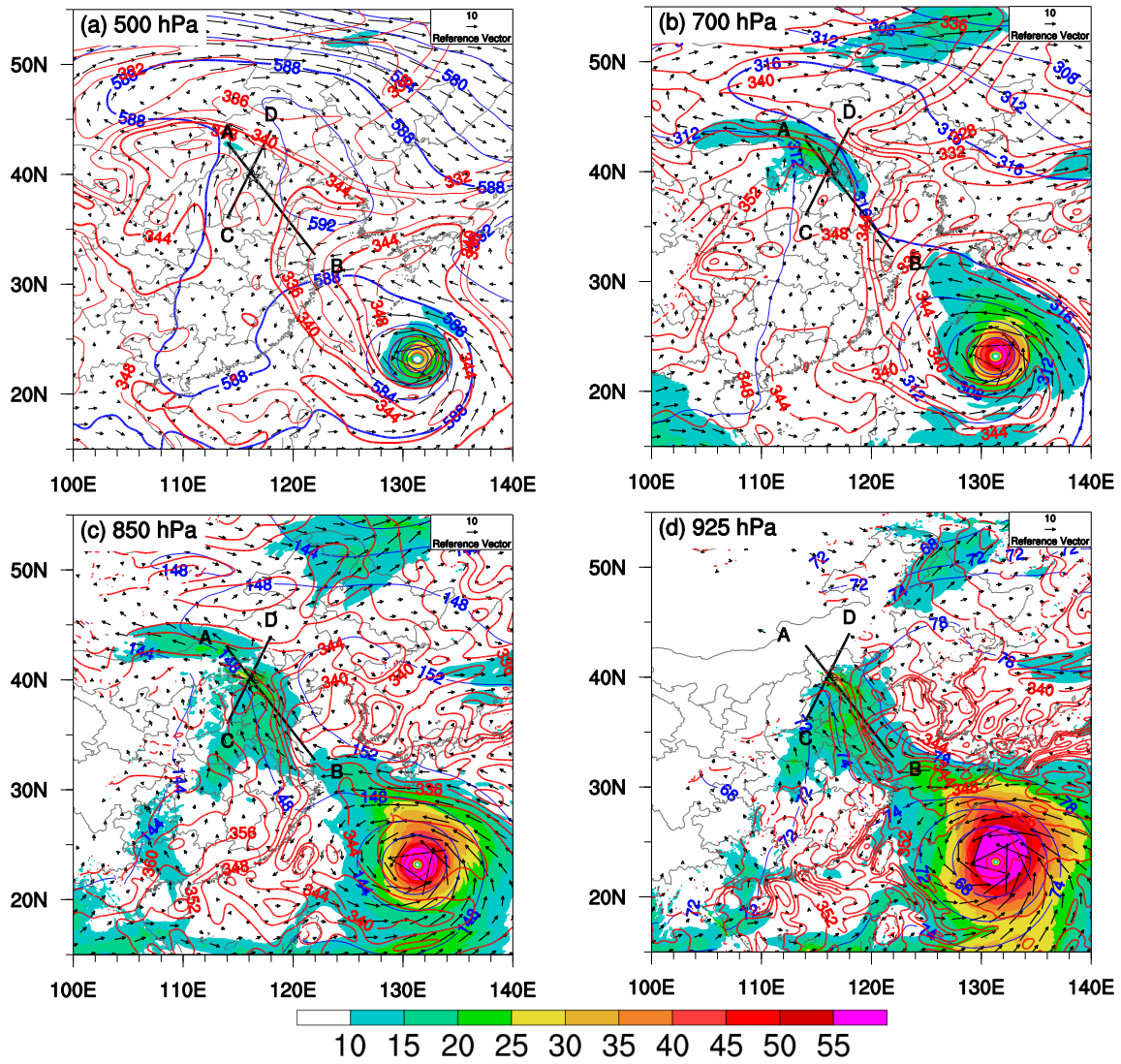
Fig. 11 Same as Fig. 9 but for 0800 UTC 31 July 2023. Thick black lines A–B and C–D denote the locations for the cross-section in Fig. 12.

As addressed above, it was the variation in environmental conditions that caused consequent rainfall changes in nature. Especially, the shift in the wind field brought changes in thermodynamic processes and water vapor sources. Before the wind shift (Figs. 9 and 10), water vapor was mainly from the East China Sea associated with the cyclonic circulation of the typhoon remnant vortex and the tropical storm Khanun and southeasterly flow below 925 hPa. After the shift, water vapor flux was significantly reduced from both southwesterly and southeasterly flows (Fig. 11). Under such a framework, convections were largely triggered by orographic blocking and lifting of southerly/southwesterly flows as convective instability air approached the orography (Fig. 12). Unlike in the first stage, convections were further developed northward over mountains, forming deep convections (Fig. 12b), which might be

379 attributed to the fact that the cold air on the north side moved northward. Generally speaking,

380 the convections in the second stage are much stronger and deeper than those in the first stage.

381 Consequently, the rainfall intensity is increased, compared to those in the first stage (Figs.

382 7d,e).

383

384
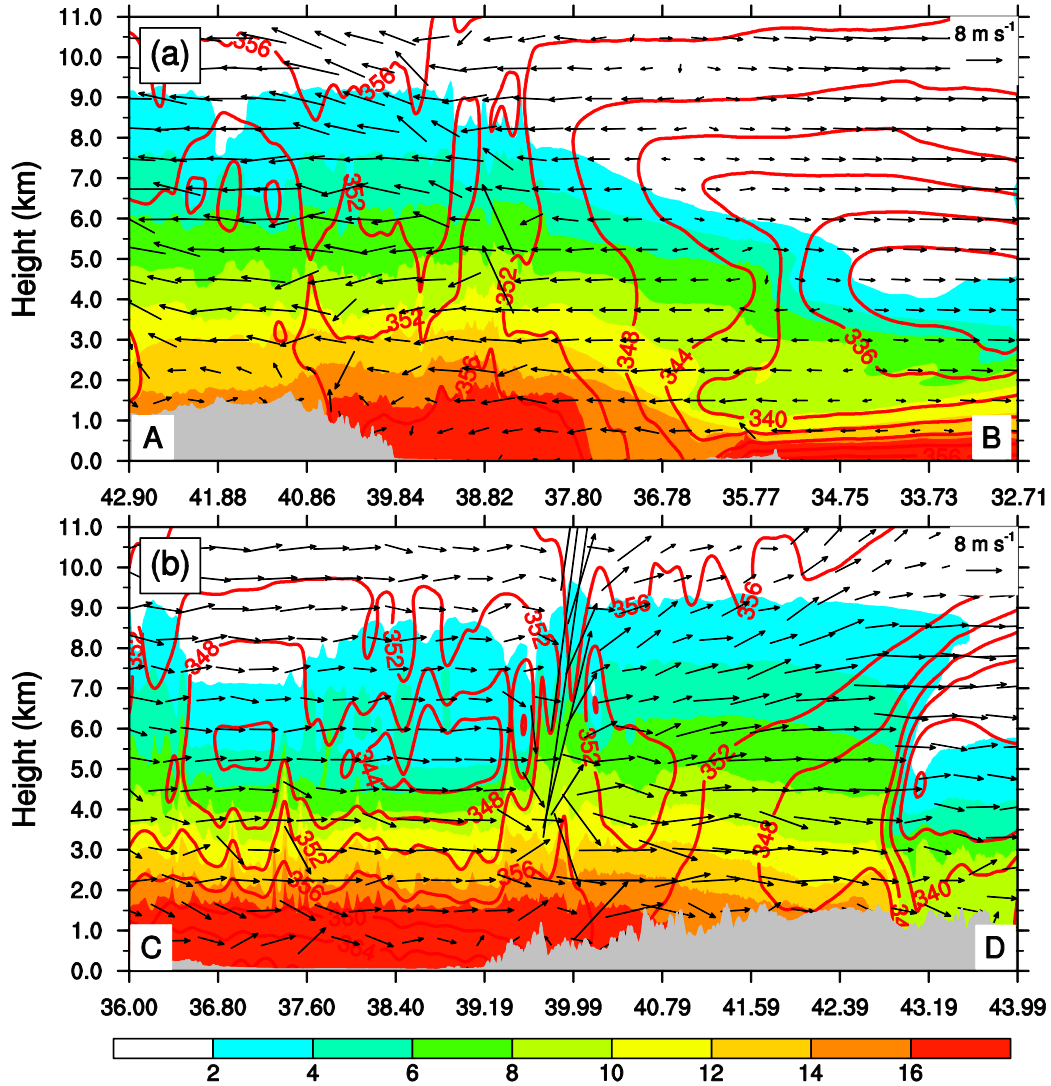
385 **Fig. 12** Vertical cross-sections along lines (a) A–B and (b) C–D given in Fig. 11 of equivalent

386 potential temperature (θ_e, red-contoured at 4K intervals), water vapor mixing ratio (q_v, g kg^{-1},

387 shadings), and in-plane flow vectors (vertical motion amplified by a factor of 10) at 0800 UCT

388 31 July 2023. Gray shadings denote terrain.

389 *4.2 Moisture budget*

390 The shift in wind direction and speed implies a change in water vapor source and rainfall

391 properties (Fig. 13). As stated above, water vapor was mainly from the East China Sea

392 associated with the cyclonic circulation of typhoon Khanun before the wind shift, and was

393   fueled by the southeasterly flow below 925 hPa. After the shift, the water vapor supply was

394   significantly reduced due to both southwesterly and southeasterly flow variations. Figure 13

395   shows the time-height cross-sections of moisture flux across eastern, southern, western, and

396   northern boundaries and total lateral boundary moisture flux for the MTG region. The

397   moisture flux is calculated by

398
$$QFlux = \int_0^L q_v \vec{v} \, dl \, .$$

399   Here, $QFlux$ is moisture flux across one of the four boundaries, and q_v, $\vec{v}$, and L are water

400   vapor mixing ratio, wind vector, and the length of the boundary, respectively. The TOT is a

401   summation of the $QFluxs$ from the four boundaries by taking inward (outward) as positive

402   (negative).

403   One can see that the MTG region experienced vigorous lower-to-middle level inward

404   (outward) moisture fluxes across their eastern and southern (western and northern) boundaries.

405   For the eastern boundary (Fig. 13a), the inward moisture flux began to increase gradually from

406   0000 UTC 29 July, with the maximum values over 13,500 kg kg^{-1} m^2 s^{-1} occurring between

407   1200 UTC 30 and 0000 UTC 31 July 2023. Then, the inward flux moisture decreased rapidly

408   and even transformed to the outward flux at 0000 UTC 1 August 2023. The inward moisture

409   flux was mainly concentrated below 3 km above the sea level because upper levels were capped

410   by the warm dry air masses associated with the WNPSH (cf. Figs. 9 and 10) movement.

411   However, owing to weak lifting over, most of the water vapor flowed out through the western

412   boundary (Fig. 13b). Meanwhile, part water vapor was transported in this region from the

413   southern boundary except for the lower levels during 0000 UTC 30 to 0000 UTC 31 July 2023

414   (Fig. 13d). The outward flow water vapor is caused by the northeasterly branch around flow

415   due to the blocking of the Yanshan Mountains. Similar patterns can be found in the northern

416   boundary with almost the same outward water vapor flux (Fig. 13c). The temporal evolution of

417   the water vapor flux across the eastern boundary is consistent with that of rainfall over this

418   region (Figs. 13a and 7d), suggesting that rainfall formation was dominated by the inward of

419   water vapor from the eastern boundary. Overall, the inward net moisture fluxes were

420   concentrated in the lower troposphere between 0.5 km and 1.5 km (Fig. 13e), suggesting that

most of the water vapor was consumed at this layer by condensation. Despite the high water vapor flux, the water vapor-rich layer is too thin (nearly 1 km) to be favorable for the formation of severe rainfall. Similar patterns can be found over both YX and XT regions (not shown), although there were temporal and quantitative differences.
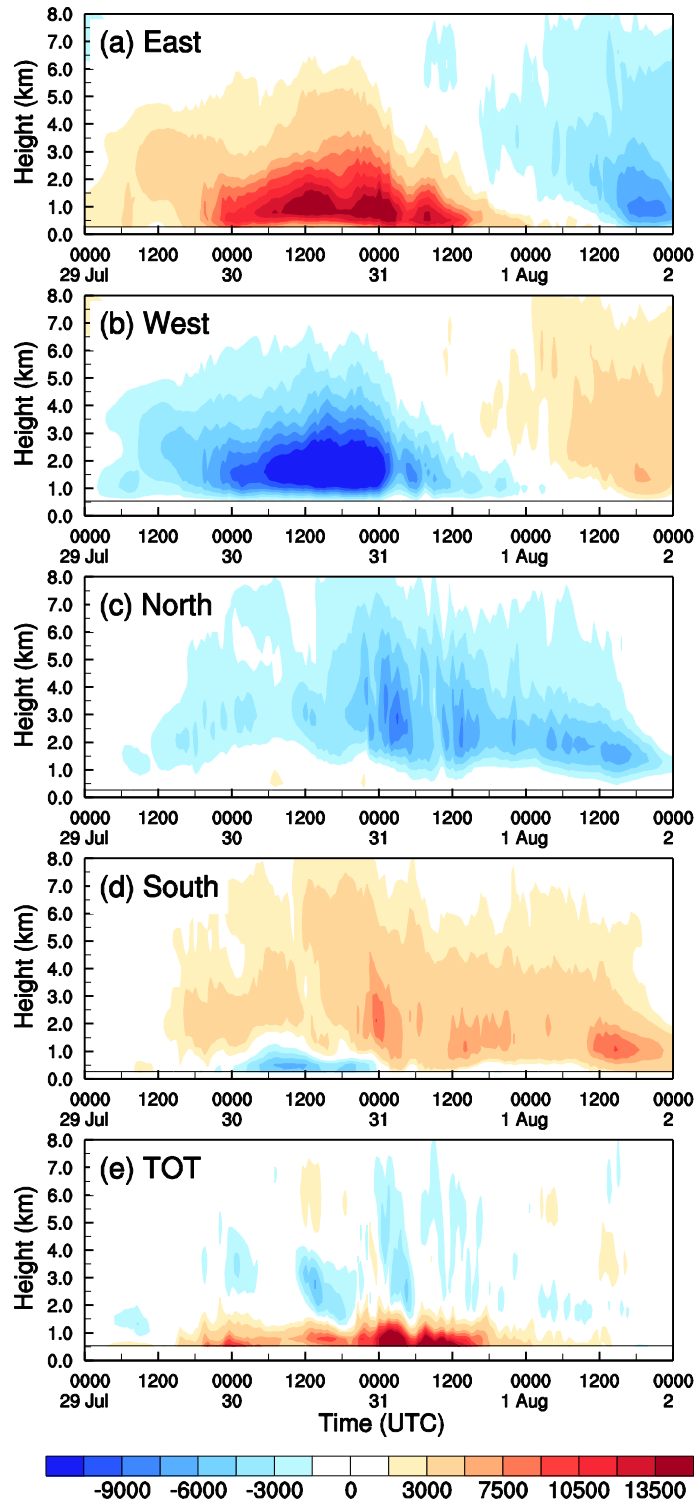
Fig. 13 Time-height cross-sections of the moisture fluxes (kg kg^{-1} m^2 s^{-1}) through the (a) eastern, (b) western, (c) northern, and (d) southern boundaries of the MTG region in Fig. 1; (e)

428   TOT provides the total net moisture flux of all boundaries.

429   In the second stage, the north-south orientated θ_e dense zone greatly prevented water vapor

430   from being transported to North China by southeasterly flows from the East China Sea, and thus

431   water vapor was mainly transported to North China across the south boundary (Figs. 13b, d).

432   Unlikely, the water vapor was mainly provided by southeasterly (southwesterly) flow

433   below(above) 500 hPa. Figure 13 shows the time-height cross-sections of the moisture fluxes.

434   It is seen from Fig. 13 that the water vapor flux amount was significantly reduced. Despite the

435   thickening of the water vapor flux layer associated with the southerly/southwesterly flows, the

436   water vapor flux is much less, compared to the first stage. Therefore, the wind shift had strong

437   effects on the reduction in water vapor flux and consequent rainfall over North China. The same

438   results can also be obtained in the YX and XT regions (not shown). It is worth emphasizing that

439   strong hourly rainfalls occurred during the wind shift period (cf. Figs. 2, 7, and 8), suggesting

440   that the changes in wind direction enhanced wind shear and thus promoted the development of

441   convections and consequent precipitation under moisture and instability conditions (Chen et al.,

442   2015; Rotunno et al.,1988; Schumacher and Rasmussen,2020). Therefore, it is important to pay

443   special attention to environmental wind alterations in future remote rainfall forecasts.

444   *4.3 Properties of convection*

445   Figure 14 shows the temporal evolution of maximum upward motion and radar reflectivity

446   over the MTG region during the rainfall period from 0000 UTC 29 to 0000 UTC 2 August 2023.

447   In the first stage (i.e., before 0800 31 July), most of the maximum updrafts were almost less

448   than 3 m s^{-1}. Owing to the weak updrafts, the storm did not stretch as high as typical convective

449   systems over North China, with hydrometeors concentrated on the levels with a temperature

450   above 0°C (Fig. 14a). As addressed above (Fig. 10), weak updrafts were attributed by the

451   unfavorable large-scale conditions. The vertical distribution of hydrometeor indicates that the

452   warm rain processes were dominant in the persistent rainfall event. The result is consistent with

453   the water vapor consumed layer between 0.5 km and 1.5 km (Fig. 13e). Unlikely, the maximum

454   updraft was over 11 m s^{-1} in the second stage (i.e., after 0800 31 July), which is much stronger

455   than that in the first stage (Fig. 14). Correspondingly, the radar reflectivity penetrated through

456   the 0°C level with a cloud top exceeding 12 km, indicating that both warm and cold rain

457 processes were active in this stage. Correspondingly, the intensity of hourly rainfall increased

458 significantly, with the maximum value exceeding 100 mm (Fig. 7d). Generally speaking, there

459 are larger strong convective areas in the second than those in the first stage. The same features

460 were also found in the regions of YX and XT (not shown). Unlike the usual short-duration

461 heavy rainfall in North China (Mao et al.,2018; Xia and Zhang,2019; Yin et al.,2022b; Li et

462 al., 2024), this precipitation was mainly dominated by warm cloud processes (Fig. 14),

463 consistent with observations (e.g., Fu et al., 2023). As addressed above, the weak updrafts

464 with warm-moist air were responsible for persistent rainfall but low intensity. A detailed

465 analysis of cloud microphysical processes for this event will be given in a forthcoming study,

466 in which all microphysical source and sink terms will be explained.

467
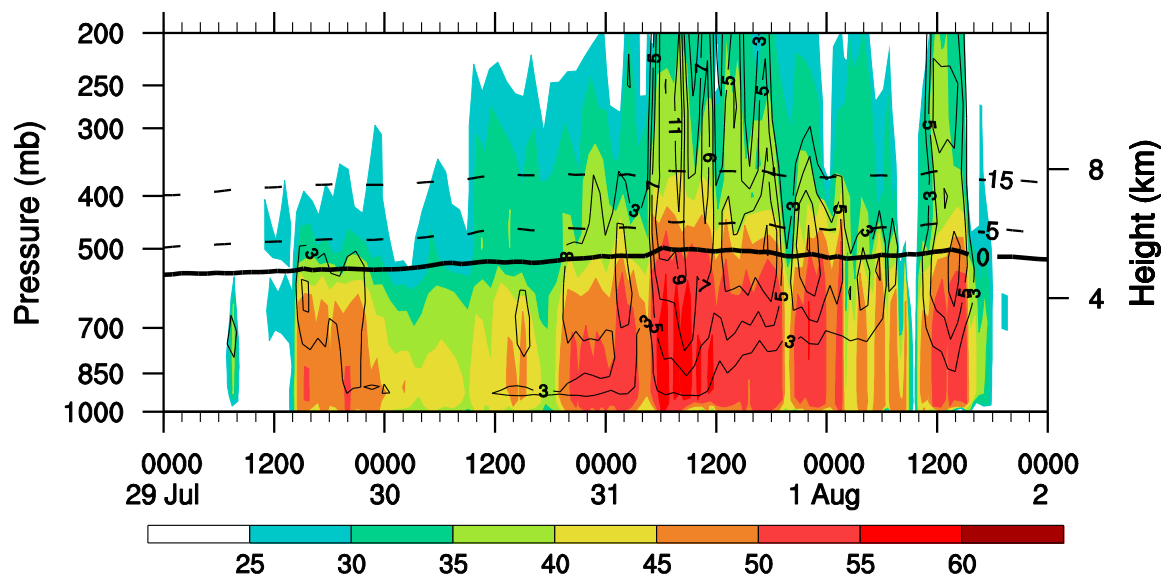
468 **Fig. 14** Time-height cross-section of domain maximum radar reflectivity (dBz, shadings) and

469 upward motion (contoured at 2 m s^{-1}) taken from MTG region during the period from 0000

470 UTC 29 to 0000 UTC 2 August 2023. The isothermal lines denote the 0°C (the melting layer),

471 -5°C, and -15°C levels, respectively.

5. Conclusions and outlook

473   In this study, we examined the convective initiation and subsequent persistent heavy

474 rainfall over North China during the period from 29 July to 2 August 2023 in terms of

475 observations and simulations with the WRF model. From observations, the rainfall was

476 featured by long duration and widespread coverage but low intensity, like a warm front rainfall.

477 Firstly, the persistent severe rainfall event was reproduced by the WRF model. Further

478   analysis based on the simulations shows that this persistent precipitation was caused by a

479   combination of a remnant vortex originating from typhoon Doksuri (2305), the tropical storm

480   Khanun (2306), the Western North Pacific subtropical high (WNPSH) with an unusual

481   westward extension of the northwestern corner, and stable cold dry air from over northern

482   China.

483   According to the simulated wind profiles and rainfall features, the persistent heavy rainfall

484   event was divided into two stages. Figure 15 summarizes the synoptic-scale forcings and

485   possible dynamic mechanisms for the persistent heavy rainfall. In the first stage (Fig. 15a), a

486   water vapor transportation passage was built by a typhoon remnant vortex and a tropical storm

487   Khanun, providing a stable warm moist water vapor supply. Several days before the rainfall

488   event, the southwestern WNPSH was within the typhoon Doksuri's outer region, and thus the

489   southwestern WNPSH was weakened by the tropical storm Doksuri. It appears that the west

490   boundary of the western North Pacific subtropical high (WNPSH) retreated eastward from 500

491   hPa to 850 hPa, showing an inclined vertical distribution on the western boundary, especially

492   from 700 hPa to 850 hPa. Capped by the inclined WNPSH, water vapor was mainly transported

493   to North China through a water vapor passage under nearly 850 hPa (Fig. 10). Although the

494   warm and moist regions were favorable for precipitation over North China, organized strong

495   convective systems were seldom because of the absence of favorable large-scale conditions. At

496   the same time, the orography in the western part of North China was occupied by dry cold air

497   mass over levels above 3.0 km. Owing to the blockings of orography below 1.3 km and the

498   strong cold air mass above 3.0 km, only the southeasterly flows between 1.3 and 3.0 km above

499   the sea level can overpass the mountains. Although the warm and moist southeasterly flows

500   were lifted by the orography, they could not go further upward to trigger convections because of

501   the locally capped cold and dry air masses overhead. Under the conditions, significant

502   equivalent potential temperature gradients were established between the warm and cold air

503   masses, similar to a warm front. Consequently, convergence mainly resulted from the changes

504   in wind direction and wind speed led to upward motion. As the warm and moist air was lifted,

505   condensation occurred and further generated precipitation. However, the lifting was too weak

506   to allow convection to be highly organized (Fig. 14), leading to the rainfall in low intensity but

507   large coverage. Besides, the continuous and stable transportation of water vapor provided by

508   tropical storm Khanun ensured stable precipitation over a long period of over 80 h. Therefore,

509   this event shows similar rainfall features to those of a warm front rainfall with a long duration

510   and widespread coverage but low intensity.

511   In the second stage (Fig. 15b), the WNPSH further expanded westward at 500 hPa, with its

512   western border reaching western China. However, the southwest part of WNPSH was further

513   damaged by the rapid intensification of Khanun into a super typhoon. Consequently, the

514   embedded warm-dry cover associated with the tilted WNPSH was significantly thinned,

515   favoring convective development. Meanwhile, as the trough deepened over northeastern China,

516   cold air from the north poured southward. Consequently, a north-south-orientated equivalent

517   potential temperature (θ_e) dense zone was established over eastern China, which greatly

518   prevented water vapor from being transported to North China (Fig. 12a). However, owing to the

519   clockwise rotated southeasterly flow, a deep southerly /southwesterly flow was built over North

520   China. The convections were triggered by orographic blocking and lifting of

521   southerly/southwesterly flows as convective instability air approached orography. Unlike the

522   first stage, the convections were further developed northward over mountains, forming deep

523   convections. It should be noted that the northward-moved cold air on the north side was

524   another favorable condition. Therefore, the convections in the second stage are much stronger

525   and deeper than those in the first stage, although water vapor flux is smaller in the second

526   period. Consequently, the rainfall intensity is increased, compared to that in the first stage.

527   Correspondingly, both warm and cold rain processes were active in the second stage, while

528   warm rain processes were dominant in the first stage.

529

530
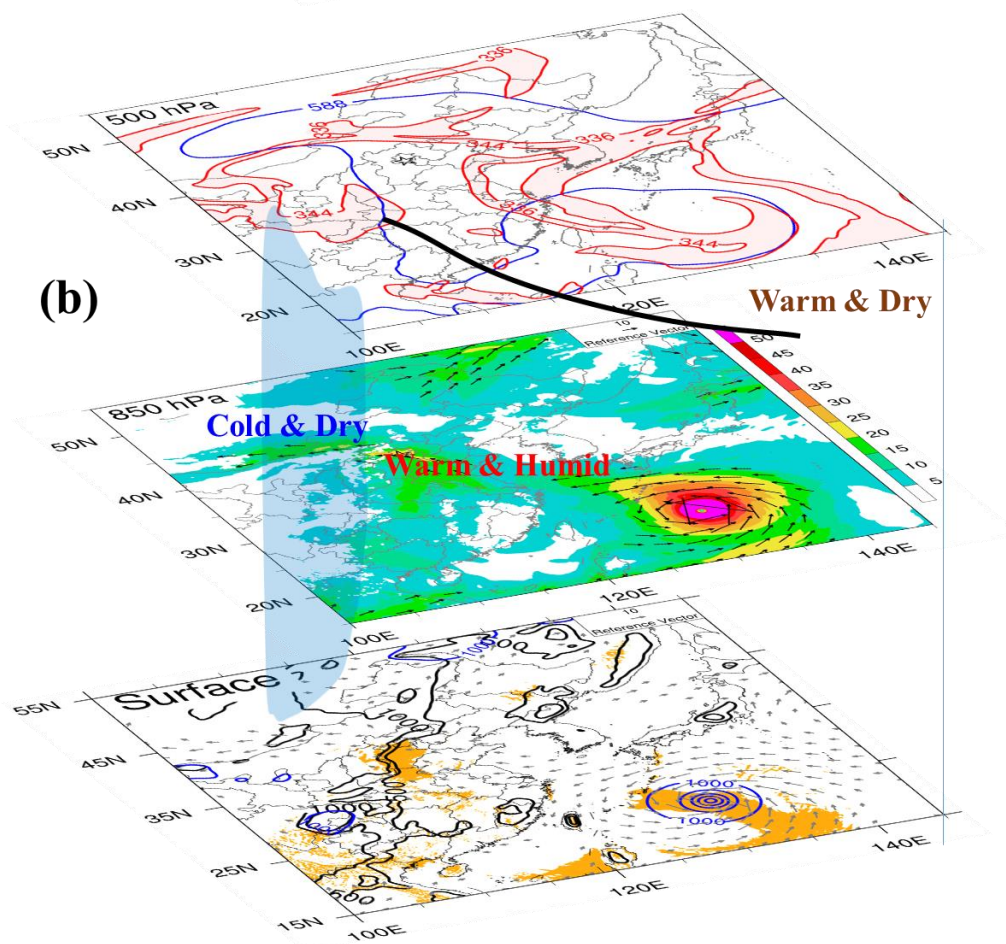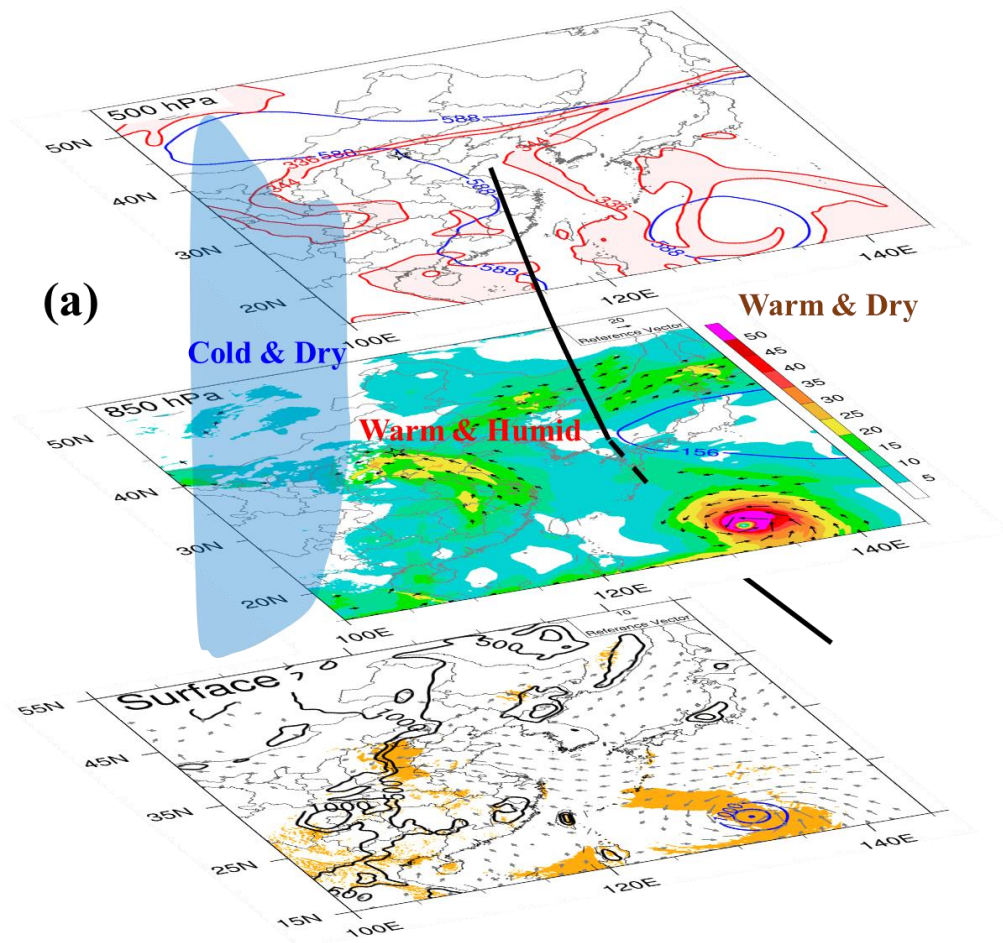
Fig. 15 (a) Three-dimensional diagram of the mechanisms for the persistent heavy precipitation in the first stage. Several distinct synoptic systems, including the tropical storm Khanun (2306), a remnant vortex originating from the typhoon Doksuri (2305), quasi-stationary cold dry air masses, and an abnormal Western North Pacific subtropical high (WNPSH) with inclined vertical distribution on the western boundary (thick black line). Blue lines marked with 588 and 156 represent the WNPSH at 500 hPa and 850 hPa, respectively. Red lines denote the spatial distribution of equivalent potential temperature (θ_e) dense zone between 336 K and 344K. At 850 hPa, black arrows indicate jets with wind speed over 12 m s^{-1}, and shadings denote water vapor flux. Orange shadings imply 96-h accumulated rainfall over 200 mm; blue contours denote sea level pressure; gray arrows denote surface (i.e., $z =10$ m) horizontal wind with wind speed over 5 m s^{-1}, and black contours indicate orography (m). (b) Same as (a) but for rainfall in the second stage.

In this study, we have gained principal results of the persistent heavy rainfall event. It is important to note that the spatial distribution of rainfall is usually considered to be consistent with the western boundary of WNPSH (i.e., the 588 isoline) at 500 hPa. In the present event, the spatial distribution of rainfall is consistent with the dense zone of θ_e, rather than the western boundary of WNPSH. Therefore, in addition to the 588 isoline, the spatial distribution of θ_e needs to be given more attention in future operational forecasts. Besides, we should give weight to environmental wind shifts, which may lead to changes in convections and the nature of consequent precipitation. Although reasonable dynamic mechanisms for the present persistent heavy rainfall have been proposed, there are still several questions that need to be answered. Among those, more work is required to understand detailed cloud and precipitation processes. In addition, diagnostic and budget analyses will be conducted to understand how the orography facilitates the generation of the rainfall belt with three rainfall cores along the mountains. Nevertheless, the concept of synoptic-forcing-based forecasting is discussed as it might apply to a broader spectrum of forecast events than just over North China.

Code and data availability

The source code of the Weather Research and Forecasting model (WRF v4.1.3) is available at https://github.com/wrf-model/WRF/releases (last access 1 August 2024). The National

562 Centers for Environmental Prediction (NCEP) Global Forecast System one-degree final

563 analysis data at 6 h intervals used for the initial and boundary conditions for the specific

564 analyzed period can be downloaded at https://rda.ucar.edu/datasets/d083002/ (last access 1

565 August 2024). Modified WRF model codes and all the data used in this study are available

566 from the authors upon request.

567

Author contributions

569 Conceptualization: JY, JS, and XL; methodology: JY and JS; data curation: JY and FL;

570 writing – original draft preparation: JY, and FL; writing – review and editing: JY, ML, RX,

571 XB, and JS; project administration: XL; funding acquisition: JY and XL. All authors have

572 read and agreed to the published version of the paper.

573

Competing interests

575 The contact author has declared that none of the authors has any competing interests.

576

Acknowledgments

578 The authors acknowledge the use of the NCAR Command Language (NCL) in the preparation

579 of figures.

580

Financial support

582 This study is jointly supported by the National Key R&D Program of China

583 (2022YFC3003903), National Natural Science Foundation of China (42075083), Open Project

584 Fund of China Meteorological Administration Basin Heavy Rainfall Key Laboratory

585 (2023BHR-Z03), Basic Research Fund of Chinese Academy of Meteorological Sciences

586 (2023Z001), and the Development Foundation of Chinese Academy of Meteorological

587 Sciences (2019KJ026).

References

588

589   Bao, X., Sun, J., Yin, J., Gao, X., Li, F., Liang, X., Gu, H., Xia, R., Li, M., Wu, C., and Feng,

590   J.: What Caused the Differences between "23·7" and "96·8" Extreme Rainfall Events in

591   North China under a Similar Synoptic Background?, Journal of Meteorological Research,

592   38, 861-879, https://doi.org/10.1007/s13351-024-3192-0, 2024.

593   Bowden, J. H., Otte, T. L., Nolte, C. G., and Otte, M. J.: Examining Interior Grid Nudging

594   Techniques Using Two-Way Nesting in the WRF Model for Regional Climate Modeling, J.

595   Clim., 25, 2805-2823, https://doi.org/10.1175/JCLI-D-11-00167.1, 2012.

596   Chen, Q., Fan, J., Hagos, S., Gustafson Jr, W. I., and Berg, L. K.: Roles of wind shear at

597   different vertical levels: Cloud system organization and properties, Journal of Geophysical

598   Research: Atmospheres, 120, 6551-6574, https://doi.org/10.1002/2015JD023253, 2015.

599   Ding, Y.: A case study on the excessively severe rainstrom in Honan province, early in August,

600   1975, Scientia Atmospherica Sinica, 2, 276-289. (in Chinese), 1978.

601   Dudhia, J.: Numerical Study of Convection Observed during the Winter Monsoon Experiment

602   Using a Mesoscale Two-Dimensional Model, Journal of the Atmospheric Sciences, 46,

603   3077-3107, https://doi.org/10.1175/1520-0469(1989)046<3077:NSOCOD>2.0.CO;2,

604   1989.

605   Feng, W. and Cheng, L.: Nonhydrostatic numerical simulation for the "96.8" extraordinary

606   rainstorm and the developing structure of mesoscale system, 16, 423-440, 2002.

607   Fowler, H. J., Blenkinsop, S., Green, A., and Davies, P. A.: Precipitation extremes in 2023,

608   Nature Reviews Earth & Environment, 5, 250-252,

609   https://doi.org/10.1038/s43017-024-00547-9, 2024.

610   Fu, J., Quan, W., Mai, Z., Luo, Q., Chen, T., Li, X., Xu, X., Zhu, W., Hua, S., and Han, X.:

611   Preliminary study on the refined characteristics of rainfall intensity and dynamic and

612   thermodynamic conditions in the July 2023 severe torrential rain in north China,

613   Meteorological Monthly, 49, 1435-1450, 10.7519/j.issn.1000-0526.2023.112701, 2023.

614   (In Chinese with English abstract)

615   Gao, Z., Zhang, J., Yu, M., Liu, Z., Yin, R., Zhou, S., Zong, L., Ning, G., Xu, X., Guo, Y., Wei,

616   H., and Yang, Y.: Role of Water Vapor Modulation From Multiple Pathways in the

617   Occurrence of a Record-Breaking Heavy Rainfall Event in China in 2021, Earth and Space

618   Science, 9, e2022EA002357, https://doi.org/10.1029/2022EA002357, 2022.

619   Gao, X., Sun, J., Yin, J., Abulikemu, A., Wu, C., Liang, X., and Xia, R.: The impact of

620   mountain-plain thermal contrast on precipitation distributions during the "23·7"

621   record-breaking heavy rainfall over North China, Atmospheric Research, 107582,

622   https://doi.org/10.1016/j.atmosres.2024.107582, 2024.

623   Hirata, H. and Kawamura, R.: Scale interaction between typhoons and the North Pacific

624   subtropical high and associated remote effects during the Baiu/Meiyu season, Journal of

625   Geophysical Research: Atmospheres, 119, 5157-5170,

626   https://doi.org/10.1002/2013JD021430, 2014.

627   Hong, S.-Y., Dudhia, J., and Chen, S.-H.: A Revised Approach to Ice Microphysical

628   Processes for the Bulk Parameterization of Clouds and Precipitation, Monthly Weather

629   Review, 132, 103-120,

630   https://doi.org/10.1175/1520-0493(2004)132<0103:ARATIM>2.0.CO;2, 2004.

631   Hu, G., Lu, M.-H., Reynolds, D., Wang, H.-K., Chen, X., Liu, W.-C., Zhu, F., Wu, X.-W., Xia,

632   F., Xie, M.-C., Cheng, X.-N., Lim, K.-S., Zhai, B.-P., and Chapman, J.: Long-term

633   seasonal forecasting of a major migrant insect pest: the brown planthopper in the Lower

634   Yangtze River Valley, J. Pest Sci., 92, https://doi.org/10.1007/s10340-018-1022-9, 2019.

635   Janjić, Z. I.: The step-mountain eta coordinate model: further developments of the convection,

636   viscous sublayer, and turbulence closure schemes, Monthly Weather Review, 122,

637   927-945, https://doi.org/10.1175/1520-0493(1994)122<0927:TSMECM>2.0.CO;2, 1994.

638   Janjić, Z. I.: Nonsingular implementation of the Mellor-Yamada Level 2.5 Scheme in the NCEP

639   Meso model. NCEP Office Note No. 437, 61 pp., 2002.

640   Jiménez, P. A., Dudhia, J., González-Rouco, J. F., Navarro, J., Montávez, J. P., and

641   García-Bustamante, E.: A Revised Scheme for the WRF Surface Layer Formulation,

642   Monthly Weather Review, 140, 898-918, https://doi.org/10.1175/MWR-D-11-00056.1,

643   2012.

Kain, J. S.: The Kain–Fritsch Convective Parameterization: An Update, Journal of Applied

Meteorology, 43, 170-181,

https://doi.org/10.1175/1520-0450(2004)043<0170:TKCPAU>2.0.CO;2, 2004.

Li, H., Yin, J., and Kumjian, M.: ZDR Backwards Arc: Evidence of Multi-Directional Size

Sorting in the Storm Producing 201.9 mm Hourly Rainfall, Geophys. Res. Lett., 51,

e2024GL109192, https://doi.org/10.1029/2024GL109192, 2024.

Li, M., Sun, J., Li, F., Wu, C., Xia, R., Bao, X., Yin, J., and Liang, X.: Precipitation Evolution

from Plain to Mountains during the July 2023 Extreme Heavy Rainfall Event in North

China, Journal of Meteorological Research, 38, 635-651, 10.1007/s13351-024-3182-2,

2024.

Lin, Y.-H. and Wu, C.-C.: Remote Rainfall of Typhoon Khanun (2017): Monsoon Mode and

Topographic Mode, Monthly Weather Review, 149, 733-752,

https://doi.org/10.1175/MWR-D-20-0037.1, 2021.

Mao, J., Ping, F., Yin, L., and Qiu, X.: A Study of Cloud Microphysical Processes Associated

With Torrential Rainfall Event Over Beijing, Journal of Geophysical Research:

Atmospheres, 123, 8768-8791, https://doi.org/10.1029/2018JD028490, 2018.

Meng, Z., Zhang, F., Luo, D., Tan, Z., Fang, J., Sun, J., Shen, X., Zhang, Y., Wang, S., Han, W.,

Zhao, K., Zhu, L., Hu, Y., Xue, H., Ma, Y., Zhang, L., Nie, J., Zhou, R., Li, S., Liu, H., and

Zhu, Y.: Review of Chinese atmospheric science research over the past 70 years: Synoptic

meteorology, Science China Earth Sciences, 62, 1946-1991,

https://doi.org/10.1007/s11430-019-9534-6, 2019.

Mlawer, E. J., Taubman, S. J., Brown, P. D., Iacono, M. J., and Clough, S. A.: Radiative transfer

for inhomogeneous atmospheres: RRTM, a validated correlated-k model for the longwave,

Journal of Geophysical Research: Atmospheres, 102, 16663-16682,

https://doi.org/10.1029/97JD00237, 1997.

Tomas, P., Pieter, G., and Ivan, T.: Vertical wind shear and convective storms,

https://doi.org/10.21957/z0b3t5mrv, 2021.

Rao, C., Chen, G., and Ran, L.: Effects of Typhoon In-Fa (2021) and the Western Pacific

672   Subtropical High on an Extreme Heavy Rainfall Event in Central China, Journal of

673   Geophysical Research: Atmospheres, 128, e2022JD037924,

674   https://doi.org/10.1029/2022JD037924, 2023.

675   Rotunno, R., Klemp, J., and Weisman, M.: A Theory for Strong, Long-Lived Squall Lines,

676   Journal of The Atmospheric Sciences - J ATMOS SCI, 45, 463-485,

677   https://doi.org/10.1175/1520-0469(1988)045<0463:ATFSLL>2.0.CO;2, 1988.

678   Schumacher, R. S. and Rasmussen, K. L.: The formation, character and changing nature of

679   mesoscale convective systems, Nature Reviews Earth & Environment, 1, 300-314,

680   10.1038/s43017-020-0057-7, 2020.

681   Stauffer, D. R., Seaman, N. L., and Binkowski, F. S.: Use of Four-Dimensional Data

682   Assimilation in a Limited-Area Mesoscale Model Part II: Effects of Data Assimilation

683   within the Planetary Boundary Layer, Monthly Weather Review, 119, 734-754,

684   https://doi.org/10.1175/1520-0493(1991)119<0734:UOFDDA>2.0.CO;2, 1991.

685   Sun, J., Qi, L., and Zhao, S.: A study on mesoscale convective systems of the severe heavy

686   rainfall in north China by "9608" typhoon, Acta Meteorologica Sinica, 64, 57-71,

687   10.11676/qxxb2006.006, 2006.

688   Sun, Y., Zhong, Z., Yi, L., Li, T., Chen, M., Wan, H., Wang, Y., and Zhong, K.: Dependence of

689   the relationship between the tropical cyclone track and western Pacific subtropical high

690   intensity on initial storm size: A numerical investigation, Journal of Geophysical Research:

691   Atmospheres, 120, 11,451-411,467, https://doi.org/10.1002/2015JD023716, 2015.

692   Tewari, M., Chen, F., Wang, W., Dudhia, J., LeMone, M. A., Mitchell, K., Ek, M., Gayno, G.,

693   Wegiel, J., and Cuenca, R. H.: Implementation and verification of the unified NOAH land

694   surface model in the WRF model. 20th conference on weather analysis and

695   forecasting/16th conference on numerical weather prediction, pp. 11-15., 2004.

696   Thompson, G., Field, P. R., Rasmussen, R. M., and Hall, W. D.: Explicit Forecasts of Winter

697   Precipitation Using an Improved Bulk Microphysics Scheme. Part II: Implementation of a

698   New Snow Parameterization, Monthly Weather Review, 136, 5095-5115,

699   https://doi.org/10.1175/2008MWR2387.1, 2008.

Wang, Y., Wang, Y., and Fudeyasu, H.: The Role of Typhoon Songda (2004) in Producing Distantly Located Heavy Rainfall in Japan, Monthly Weather Review, 137, 3699-3716, https://doi.org/10.1175/2009MWR2933.1, 2009.

Xia, R., Ruan, Y., Sun, J., Liang, X., Li, F., Wu, C., Li, J., Yin, J., Bao, X., Li, M., and Gao, X.: Distinct Mechanisms Governing Two Types of Extreme Hourly Rainfall Rates in the Mountain Foothills of North China During the Passage of a Typhoon Remnant Vortex from July 30 to August 1, 2023, Advances in Atmospheric Sciences, https://doi.org/10.1007/s00376-024-4064-3, 2025.

Xia, R. and Zhang, D.-L.: An Observational Analysis of Three Extreme Rainfall Episodes of 19–20 July 2016 along the Taihang Mountains in North China, Monthly Weather Review, 147, 4199-4220, https://doi.org/10.1175/MWR-D-18-0402.1, 2019.

Xu, H. and Li, X.: Torrential rainfall processes associated with a landfall of Typhoon Fitow (2013): A three-dimensional WRF modeling study, Journal of Geophysical Research: Atmospheres, 122, 6004-6024, https://doi.org/10.1002/2016JD026395, 2017.

Xu, H., Zhang, D., and Li, X.: The Impacts of Microphysics and Terminal Velocities of Graupel/Hail on the Rainfall of Typhoon Fitow (2013) as Seen From the WRF Model Simulations With Several Microphysics Schemes, Journal of Geophysical Research: Atmospheres, 126, e2020JD033940, https://doi.org/10.1029/2020JD033940, 2021.

Xu, H., Li, X., Yin, J., and Zhang, D.: Predecessor Rain Events in the Yangtze River Delta Region Associated with South China Sea and Northwest Pacific Ocean (SCS-WNPO) Tropical Cyclones, Advances in Atmospheric Sciences, 40, 1021-1042, https://doi.org/10.1007/s00376-022-2069-3, 2023a.

Xu, H., Zhao, D., Yin, J., Duan, Y., Gao, W., Li, Y., and Zhou, L.: Indirect Effects of Binary Typhoons on an Extreme Rainfall Event in Henan Province, China From 19 to 21 July 2021. 3. Sensitivities to Microphysics Schemes, Journal of Geophysical Research: Atmospheres, 128, e2022JD037936, https://doi.org/10.1029/2022JD037936, 2023b.

Yang, L., Liu, M., Smith, J. A., and Tian, F.: Typhoon Nina and the August 1975 Flood over Central China, Journal of Hydrometeorology, 18, 451-472,

728   https://doi.org/10.1175/JHM-D-16-0152.1, 2017.

729 Yin, J., Liang, X., Wang, H., and Xue, H.: Representation of the autoconversion from cloud to

730   rain using a weighted ensemble approach: a case study using WRF v4.1.3, Geosci. Model

731   Dev., 15, 771-786, https://doi.org/10.5194/gmd-15-771-2022, 2022a.

732 Yin, J., Zhang, D.-L., Luo, Y., and Ma, R.: On the Extreme Rainfall Event of 7 May 2017 Over

733   the Coastal City of Guangzhou. Part I: Impacts of Urbanization and Orography, Monthly

734   Weather Review, 148, 955-979, https://doi.org/10.1175/MWR-D-19-0212.1, 2020.

735 Yin, J., Gu, H., Yu, M., Bao, X., Xie, Y., and Liang, X.: Synergetic Roles of Dynamic and Cloud

736   Microphysical Processes in Extreme Short-Term Rainfall: A Case Study, Quarterly

737   Journal of the Royal Meteorological Society, 148, 3660- 3676,

738   https://doi.org/10.1002/qj.4380, 2022b.

739 Yin, J., Wang, D., Liang, Z., Liu, C., Zhai, G., and Wang, H.: Numerical Study of the Role of

740   Microphysical Latent Heating and Surface Heat Fluxes in a Severe Precipitation Event in

741   the Warm Sector over Southern China, Asia-Pacific Journal of Atmospheric Sciences, 54,

742   77-90, https://doi.org/10.1007/s13143-017-0061-0, 2018.

743 Yin, J., Gu, H., Liang, X., Yu, M., Sun, J., Xie, Y., Li, F., and Wu, C.: A Possible Dynamic

744   Mechanism for Rapid Production of the Extreme Hourly Rainfall in Zhengzhou City on 20

745   July 2021, Journal of Meteorological Research, 36, 6-25,

746   https://doi.org/10.1007/s13351-022-1166-7, 2022c.